IOP Conf. Series: Materials Science and Engineering **304** (2018) 012004 doi:10.1088/1757-899X/304/1/012004

A deterministic model of electron transport for electron probe microanalysis

J Bünger[1], S Richter[2] and M Torrilhon[1]

[1] RWTH Aachen University, Centre for Computational Engineering Science (MathCCES), Schinkelstrasse 2, 52062 Aachen, Germany
[2] RWTH Aachen University, Central Facility for Electron Microscopy (GFE), Ahornstrasse 55, 52074 Aachen, Germany

E-mail: buenger@mathcces.rwth-aachen.de

Abstract. Within the last decades significant improvements in the spatial resolution of electron probe microanalysis (EPMA) were obtained by instrumental enhancements. In contrast, the quantification procedures essentially remained unchanged. As the classical procedures assume either homogeneity or a multi-layered structure of the material, they limit the spatial resolution of EPMA. The possibilities of improving the spatial resolution through more sophisticated quantification procedures are therefore almost untouched. We investigate a new analytical model (M_1-model) for the quantification procedure based on fast and accurate modelling of electron-X-ray-matter interactions in complex materials using a deterministic approach to solve the electron transport equations. We outline the derivation of the model from the Boltzmann equation for electron transport using the method of moments with a minimum entropy closure and present first numerical results for three different test cases (homogeneous, thin film and interface). Taking Monte Carlo as a reference, the results for the three test cases show that the M_1-model is able to reproduce the electron dynamics in EPMA applications very well. Compared to classical analytical models like XPP and PAP, the M_1-model is more accurate and far more flexible, which indicates the potential of deterministic models of electron transport to further increase the spatial resolution of EPMA.

1. Introduction

Electron probe microanalysis (EPMA) provides a popular method to obtain quantitative information about the chemical composition of heterogeneous materials, particularly fine structures and grains in metals and alloys. As an imaging technique, it poses an inverse problem, as the chemical concentrations are not measured directly, but have to be reconstructed from intensity measurements of X-rays.

Usually, the experimental intensities are normalised to so-called k-ratios k^{Exp} and the simulation of a forward model provides computed k-ratios $k^{\mathrm{M}}(c)$ that depend on one or more assumed elemental concentration fields $c(x)$ inside the probe. The inverse problem [1,2] consists of finding the concentration c^* that minimises the error between the experimental and simulated k-ratios k^{M}.

Problem 1 (Inverse problem)
Find c^* such that

$$c^* = \arg\min_c \|k^{\mathrm{M}}(c) - k^{\mathrm{Exp}}\|^2 \tag{1}$$

with some appropriate norm $\|\cdot\|$.

Obviously, the reconstructed concentration $c(x)$ inherits fundamental characteristics like accuracy or assumptions on the material structure from the forward model used to compute $k^{\mathrm{M}}(c)$. Moreover, the forward model substantially determines complexity and computational cost of the inverse problem. Therefore, the choice of the forward model $k^{\mathrm{M}}(c)$ is crucial for both computational speed and accuracy of the reconstruction of concentrations $c(x)$.

Most analytical methods used nowadays use simple forward models, which either assume that the sample is homogeneous within the interaction volume [3, 4], or are based on the calculation of the $\phi(\rho z)$ distribution [5–9], where the latter model the probability of ionisation as a function of depth, expressed in mass thickness. Both types impose strong restrictions on the range of material structures to which they can be applied. The former are only applicable to structures that exceed the interaction volume and the latter require the composition to only vary as a function of depth, like thin films or multi-layers. One approach to improve the spatial resolution of EPMA is to use forward models with less or no restriction on the material structure.

When more complex concentration distributions are of interest, Monte Carlo simulations of the electrons inside the probe typically replace analytical models [10–14]. While these simulations exhibit very good physical accuracy, they are also computationally expensive and suffer from statistical noise. This makes the solution of the inverse problem to recover the chemical composition difficult.

Hence, we believe that more sophisticated forward models that balance computational effort with accuracy have to be developed in order to improve the spatial resolution of EPMA. Attempts on deterministic modelling of electrons inside solids to predict characteristic quantities like backscattered electrons and emitted X-rays used in quantitative EPMA have been made earlier [15] and similar approaches to modelling particle transport are also common in nuclear engineering [16] and electron radiotherapy [17, 18].

This paper investigates a new forward model for the prediction of local ionisation intensity for arbitrary concentration distributions, which conceptually is found between analytical models and Monte Carlo simulations. It uses a deterministic reduction technique to solve the electron transport equation as a partial differential equation. The reduction is based on the minimum entropy approach [19–21], yielding closed moment equations from the Boltzmann equation for electron transport in the continuous slowing down approximation. The simplest case is given by the so-called M_1 model, which computes the local electron energy distribution directly in a deterministic noise-free way. This allows a very efficient computation of the local ionisation intensity and also allows to use modern optimisation techniques for partial differential equations to solve the inverse problem (eq. (1)).

2. Transport theory

2.1. Boltzmann equation for electron transport

The starting point for the derivation of the model is the Boltzmann equation for electron transport, which follows from balancing the physical processes influencing the number of

electrons n with velocity v at space point x and time t in a stationary background medium

$$\begin{aligned}\frac{\partial}{\partial t}n(x,v,t) + \underbrace{v\cdot\nabla_x n(x,v,t)}_{\text{in-/outflow}} = &\underbrace{\int_{\mathbb{R}^3} N_V(x)\hat{\sigma}(x,\|v'\|,\|v\|,v'\cdot v)\|v'\|n(x,v',t)dv'}_{\text{in-scattering}} \\ &- \underbrace{\int_{\mathbb{R}^3} N_V(x)\hat{\sigma}(x,\|v\|,\|v'\|,v\cdot v')\|v\|n(x,v,t)dv'}_{\text{out-scattering}}.\end{aligned} \tag{2}$$

The solution $n : \mathbb{R}^3\times\mathbb{R}^3\times\mathbb{R}_{\geq 0}\to\mathbb{R}_{\geq 0}$ is a phase density, such that $n(x,v,t)$ is the probability density of finding an electron at position x with velocity v at time t. The background medium is modelled by $N_V(x)$, the number density of scattering centres at position x, and the scattering cross-section $\hat{\sigma}(x,\|v'\|,\|v\|,v'\cdot v)$, describing the probability that an electron changes its velocity from v' to v when hitting a scattering centre at space point x. Note that we assume the background material to be isotropic, as the scattering cross-section $\hat{\sigma}$ does not depend on the pre- and post-collision velocity vectors v' and v separately but only on the magnitudes and the angle between both vectors.

In the context of EPMA, the time scale of the physical processes is very small compared to the duration of the measurement. Therefore, we can assume that the distribution of electrons inside the material reaches a steady state immediately after switching on the electron beam and thus neglect the time dependency ($\partial/\partial_t\cdot = 0$).

Before deriving the reduced model it is convenient to rewrite eq. (2). First, we perform a transformation to energy and direction by expressing the velocity and scattering cross-section as functions of energy ϵ and direction Ω

$$v(\epsilon,\Omega) = \|v(\epsilon)\|\Omega \tag{3}$$

$$\sigma(x,\epsilon',\epsilon,\Omega'\cdot\Omega) = \hat{\sigma}(x,\|v(\epsilon')\|,\|v(\epsilon)\|,v(\epsilon')\cdot v(\epsilon)). \tag{4}$$

We then split the scattering cross-section into an elastic ($\epsilon' = \epsilon$) and an inelastic ($\epsilon' > \epsilon$) part ($\sigma = \sigma_{\text{el}} + \sigma_{\text{in}}$). Finally we define

$$\psi(x,\epsilon,\Omega) \coloneqq \|v(\epsilon)\|n(x,v(\epsilon,\Omega)) \tag{5}$$

and obtain

$$\begin{aligned}\Omega\cdot\nabla_x\psi(x,\epsilon,\Omega) = &N_V(x)\int_\epsilon^\infty\int_{S^2}\sigma_{\text{in}}(x,\epsilon',\epsilon,\Omega\cdot\Omega')\psi(x,\epsilon',\Omega')d\Omega'd\epsilon' \\ &+ N_V(x)\int_{S^2}\sigma_{\text{el}}(x,\epsilon,\Omega\cdot\Omega')\psi(x,\epsilon,\Omega')d\Omega' \\ &- N_V(x)\sigma_{\text{in}}^{\text{tot}}(x,\epsilon)\psi(x,\epsilon,\Omega) \\ &- N_V(x)\sigma_{\text{el}}^{\text{tot}}(x,\epsilon)\psi(x,\epsilon,\Omega)\end{aligned} \tag{6}$$

with the total scattering cross-sections $\sigma_{\text{el}}^{\text{tot}}(x,\epsilon) = 2\pi\int_{-1}^1\sigma_{\text{el}}(x,\epsilon,\mu)d\mu$ and $\sigma_{\text{in}}^{\text{tot}}(x,\epsilon) = 2\pi\int_0^\epsilon\int_{-1}^1\sigma_{\text{in}}(x,\epsilon,\epsilon',\mu)d\mu d\epsilon'$ where $\mu = \cos(\theta)$ with θ being the deflection angle. S^2 denotes the sphere with radius one (unit 2-sphere) and accordingly the integral over S^2 in (6) is over all directions Ω'. ψ can be interpreted as an electron fluence in the sense that $\psi(x,\epsilon,\Omega)d\Omega d\epsilon dAdt$ corresponds to the number of electrons that traverse an area dA perpendicular to Ω with a direction within the solid angle $d\Omega$ around Ω at an energy within $[\epsilon,\epsilon+d\epsilon]$ at point x during dt.

2.2. Continuous slowing down approximation
As a first simplification, the continuous slowing down approximation for the energy loss of the electrons is used. The same simplification appears in all analytical models and almost all Monte Carlo models, e.g., [11, 13]. The simplification is based on the assumption that an electron loses a significant amount of energy through a very large number of collisions, with any single collision changing the energy of the electron only slightly. In this case, the inelastic scattering cross-section is peaked about small energy losses and an asymptotic analysis with respect to energy on the inelastic in-scattering term in eq. (6) yields the following approximation

$$\begin{aligned} N_V(x) \int_\epsilon^\infty \int_{S^2} \sigma_{\text{in}}(x, \epsilon', \epsilon, \Omega \cdot \Omega') \psi(x, \epsilon', \Omega') d\Omega' d\epsilon' \\ \approx N_V(x) \int_{S^2} \sigma_{\text{in}}^{CSD}(x, \epsilon, \Omega \cdot \Omega') \psi(x, \epsilon, \Omega') d\Omega' + \frac{\partial}{\partial \epsilon}(S(x, \epsilon)\psi(x, \epsilon, \Omega)) \end{aligned} \tag{7}$$

with

$$\sigma_{\text{in}}^{CSD}(x, \epsilon, \mu) := \int_0^\infty \sigma_{\text{in}}(x, \epsilon, \epsilon', \mu) d\epsilon' \qquad S(x, \epsilon) := 2\pi \int_0^\infty \int_{-1}^1 (\epsilon - \epsilon') \sigma_{\text{in}}(x, \epsilon, \epsilon', \mu) d\mu d\epsilon'.$$

Insertion of the approximation eq. (7) into eq. (6) results in the Boltzmann equation in continuous slowing down approximation (BCSD). The term $-\partial/\partial_\epsilon(S\psi)$ can be interpreted as a transfer from higher to lower energies, with the stopping power S governing the speed of this transfer.

3. Continuum approximation
Knowing the electron fluence ψ we can compute the intensity of a specific characteristic X-ray generated at point x from (cf. [22])

$$I_{0,j}(x) = w_j \; N_{V,j}(x) \int_0^\infty \sigma_{\text{ion},j}(x, \epsilon) \int_{S^2} \psi(x, \epsilon, \Omega) d\Omega d\epsilon \tag{8}$$

where w_j and $\sigma_{\text{ion},j}$ are the fluorescence yield and ionisation cross-section of some chemical element identified by j. Note that detailed information about the angular distribution of the electron fluence ψ is not necessary to evaluate eq. (8), as only the average in angle of ψ is required. This, and the fact that solving the BCSD is computationally very expensive due to the high dimensionality of ψ, motivates further simplification with respect to the direction variable Ω.

3.1. Method of moments
The method of moments is a mathematical concept to reduce the dimension of the phase space in differential equations by integrating out selected independent variables of the phase space. Its objective is to derive equations for weighted integrals of the unknown, the so-called moments, and solve for these instead. As we want to eliminate the direction Ω, our moments of interest are integrals of ψ over the unit 2-sphere weighted by polynomials of the direction Ω

$$\psi^{(n)}(x, \epsilon) := \int_{S^2} \underbrace{\Omega \otimes \ldots \otimes \Omega}_{\text{n times}} \psi(x, \epsilon, \Omega) d\Omega. \tag{9}$$

The moment equations follow from multiplying the BCSD equation with monomials in Ω, integrating over the unit 2-sphere and identifying the moments. Here, we choose the simplest

case of only the first two moments and therefore consider moments of up to first order ($n = 0, 1$) for which we get the following moment equation system

$$-\frac{\partial}{\partial\epsilon}(S(x,\epsilon)\psi^{(0)}(x,\epsilon)) + \nabla_x\psi^{(1)} = 0 \tag{10}$$

$$-\frac{\partial}{\partial\epsilon}(S(x,\epsilon)\psi^{(1)}(x,\epsilon)) + \nabla_x\psi^{(2)} = -T\psi^{(1)} \tag{11}$$

with

$$T(x,\epsilon) \coloneqq 2\pi N_V(x)\int_{-1}^{1}(1-\mu)\left(\sigma_{\mathrm{el}}(x,\epsilon,\mu)\int_0^\infty \sigma_{\mathrm{in}}(x,\epsilon',\epsilon,\mu)d\epsilon'\right)d\mu. \tag{12}$$

Note that the zeroth moment $\psi^{(0)}$ corresponds to the integral of ψ in eq. (8). Hence, the theory computes essentially only the quantity of interest. Due to the divergence-term in the BCSD equation, the system of moment equations contains higher order moments and is thereby underdetermined. In order to obtain a closed system of partial differential equations, a closure relation that expresses the highest order moments as a function of the moments of interest

$$\psi^{(2)} = \psi^{(2)}(\psi^{(0)}, \psi^{(1)}) \tag{13}$$

has to be defined. The closure is crucial for the accuracy and mathematical properties of the moment equation system and should be chosen carefully.

3.2. Minimum entropy closure

The minimum entropy closure is physically motivated. It can be thought of as choosing the electron fluence ψ such that it minimises the Boltzmann entropy for a one particle system while generating a given set of moments $\psi^{(i)}$ $i = 0, \ldots, n$ and using it to close the system of moment equations by simply evaluating the integral expression of the highest moment.

Problem 2 (Minimum entropy closure)

1. Find ψ_{ME} so that

$$\psi_{\mathrm{ME}} = \arg\min_{\psi}\left(-\int_{S^2}\psi\log(\psi)d\Omega\right) \quad \text{such that} \quad \int_{S^2}\Omega^i\psi_{\mathrm{ME}}d\Omega = \psi^{(i)} \quad 0 \le i \le n \tag{14}$$

2. Compute $\psi^{(n+1)}$ from ψ_{ME}

$$\psi_{ME}^{(n+1)}(x,\epsilon) = \int_{S^2}\Omega^{(n+1)}\psi_{\mathrm{ME}}(x,\epsilon,\Omega)d\Omega. \tag{15}$$

This procedure yields the so-called M_1-model for electron transport [19–21]. Figure 1(a) visualises a histogram for the direction of travel of electrons in a homogeneous sample generated during a Monte Carlo simulation. The sample is subdivided into rectangular cells with each cell containing a group of lines. The lines visualise the direction of travel distribution in the cell by pointing in the corresponding direction (taking the cell centre as starting point) and having a length proportional to the number of electrons moving in this direction. For a better orientation, the mean energy of electrons is plotted in the background. From fig. 1(a), it is clear that the electrons are in a well structured configuration, enforced by the electron beam, when entering the sample. As the electrons penetrate the material they are deflected through collisions and the direction of travel distribution is more and more spread over all directions. Minimisation of the mathematical entropy corresponds to maximising the disorder of the electrons with respect

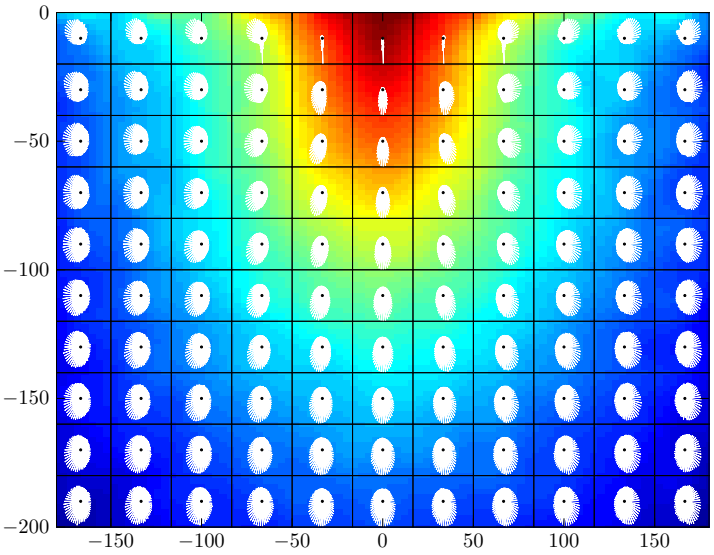

(a) Cellwise normalized direction of travel distribution

(b) $(x, z) = (0\text{nm}, -60\text{nm})$

(c) $(x, z) = (0\text{nm}, -175\text{nm})$

Figure 1. (a) Normalised direction of travel distribution of electrons in copper with $\epsilon \in [5\,\text{keV}, 10\,\text{keV}]$ obtained from a Monte Carlo simulation in DTSA-II [13,23]. (b) and (c) Angular distribution at two different depths in the Monte Carlo simulation from subfigure (a) compared to the M_1 reconstruction ψ_{M_1} and M_2 reconstruction ψ_{M_2}.

to the direction of travel for a given set of moments. This assumption of maximal disorder is not accurate over the whole range of energies. Nevertheless, the angular distribution of electrons is not rich in detail, having only one dominant direction of travel in each cell. We will show in section 4 that the M_1-model is able to reproduce the electron transport in the context of EPMA well. Figures 1(b) and 1(c) show the direction of travel distribution at two different space points, one close to the surface and another at deeper into the sample, as well as the M_1 and M_2 distribution reconstructed from the moments. As expected the minimum entropy reconstruction is better far inside the material than close to the surface. Figures 1(b) and 1(c) furthermore illustrate the improvement of the reconstruction when increasing the number of considered moments.

3.3. M_1-model

For the case of taking only the first two moments the minimum entropy closure problem for the second order moment $\psi^{(2)}$ can be solved analytically and we find

$$\psi^{(2)}_{\text{ME}} = \psi^{(0)} \left(\frac{1 - \chi(\|\alpha\|)}{2} I + \frac{3\chi(\|\alpha\|) - 1}{2} \frac{\alpha}{\|\alpha\|} \otimes \frac{\alpha}{\|\alpha\|} \right) \tag{16}$$

where χ is the Eddington factor which depends implicitly on the Euclidean norm of the anisotropy parameter $\alpha = \psi^{(1)}/\psi^{(0)}$ [19–21, 24]. The M_1-model now follows from closing the moment eqs. (10) and (11) with the minimum entropy closure relation for $\psi^{(2)}$ given by eq. (16). We define a variable vector

$$U(x, \epsilon) := (\psi^{(0)}(x, \epsilon), \psi^{(1)}(x, \epsilon)) \tag{17}$$

and write the M_1 equations in a compact form to point out the similarity to classical conservation laws with relaxation [25]

$$-\frac{\partial}{\partial\epsilon}(S(x,\epsilon)U(x,\epsilon)) + \nabla_x \cdot F(U(x,\epsilon)) = T(x,\epsilon)U(x,\epsilon) \tag{18}$$

with

$$F(U) \coloneqq \begin{pmatrix} U_1^T \\ \psi_{\mathrm{ME}}^{(2)}(U_0,\ U_1) \end{pmatrix} \qquad T(x,\epsilon) \coloneqq \begin{pmatrix} 0 & 0 \\ 0 & -T(x,\epsilon)I \end{pmatrix}.$$

Compared to classical evolution equations, $\partial/\partial_\epsilon(SU)$ takes the part of a time derivative describing an evolution of U in energy space from high to low energies. The highest possible energy is the beam energy ϵ_b, hence the initial condition is given by $U(x,\epsilon_b)$, which we approximate by Gaussian distributions centred at the point where the beam electrons enter the material. For the solution of such initial value problems, a variety of well-established numerical methods is available [25]. We decided to employ the discontinuous Galerkin (DG) method for the discretisation in space with a Runge-Kutta (RK) time stepping scheme for the integration in time [26–28]. The results presented in the following section were obtained using a second order discretisation.

At this point, our focus is to study the accuracy of the M_1-model and its numerical solutions. We therefore developed our current M_1-solver with respect to flexibility using the finite element library deal.II [29, 30]. Yet the long-term objective is to develop a M_1-solver tailored to EPMA application to efficiently solve the inverse problem.

4. Results and discussion

Although the M_1-model is designed for complex geometries, we first assess simple samples to study its validity, as more data is available for these geometries. We take results obtained from Monte Carlo (MC) simulations as reference solutions since this method can model the electron transport most accurately. The reference solutions presented in this section were generated using the DTSA-II MC software [23], which also implies the CSD approximation. A more precise physical model is implemented in the Monte Carlo code PENELOPE [14], which we plan to use for the generation of additional reference solutions in the future. In order for the comparison between the M_1- and MC-model to be as fair as possible, we use the same data for material parameters (elastic scattering cross-section, shell ionisation cross-section, etc.) in both models and therefore favour data available for both models over more elaborated data available only in DTSA-II. Table 1 gives an overview of the material models used in the simulation results presented in this section. The setups of the three test cases we will look at in this section are shown in table 2. In all test cases, we approximate the initial electron distribution as a Gaussian distribution with a standard deviation of 10 nm, corresponding to a full width at half maximum (FWHM) of approximately 23.5 nm.

The test cases are two dimensional in the sense that the systems are homogeneous in the third direction. Note that the electrons still move in three dimensions in space but their phase space distribution function is constant along one spatial direction.

At this point we study only the most essential processes, namely the electron-transport and the related generation of X-rays in the material, and leave modelling of X-ray transport and associated fluorescence effects to the future.

Table 1. Material models used in M_1 and MC simulations.

	M_1-model	MC-model
Elastic scattering cross-section	Screened Rutherford [31] (McKinley-Feshbach formula [33])	Screened Rutherford [31] (NIST Mott [32])
Stopping power	Bethe formula [31]	Bethe formula [31]
Mean ionisation potential	Sternheimer64 [34]	Sternheimer64 [34]
Absolute ionisation cross-section	Casnati82 [35]	Casnati82 [35]
X-Ray transition probability	ENDLIB-97 [36]	ENDLIB-97 [36]

Table 2. Setup of three test cases (homogeneous, thin film and interface).

Setup of test case 1 (homogeneous material)

Beam energy ϵ_B:	12, 20 keV
Beam diameter D_B:	10 nm
Material (density) El_1:	Cu ($8.96 \cdot 10^3$ kgm^{-3})

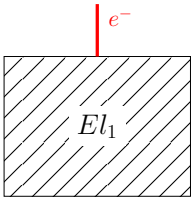

Setup of test case 2 (thin film)

Beam energy ϵ_B:	10 keV
Beam diameter D_B:	10 nm
Film thickness L:	100 nm
Material (density) El_1:	Cr ($7.2 \cdot 10^3$ kgm^{-3})
	Al ($2.7 \cdot 10^3$ kgm^{-3})
Material (Density) El_2:	Ni ($8.9 \cdot 10^3$ kgm^{-3})

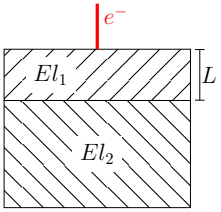

Setup of Test Case 3 (Interface)

Beam energy ϵ_B:	10 keV
Beam diameter D_B:	10 nm
Material (density) El_1:	Cr ($7.2 \cdot 10^3$ kgm^{-3})
Material (density) El_2:	Ni ($8.9 \cdot 10^3$ kgm^{-3})

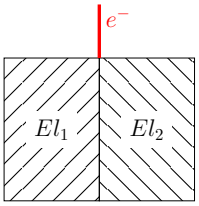

4.1. Homogeneous material

In order to start with the simplest material structure possible, we consider a homogeneous bulk of copper excited by a narrow Gaussian electron beam for different energies. As most methods for computing the k-ratios of homogeneous samples are based on the calculation of the depth distribution of radiation ($\phi(\rho z)$ curve), we use it as basis for the validation of the M_1-model here. Figure 2 shows the depth distributions of Cu-$K\alpha$ radiation computed from the M_1- and MC-model.

In addition to the M_1 and MC solutions, we added the depth distributions obtained with two common analytical models, the XPP [9] and the PAP [4] model. For a better comparability, the M_1 and MC results are scaled such that the maximum value of the depth distribution is equal to the maximum value of the PAP depth distribution. Note that the scaling corresponds to changing the number of simulated electrons and thereby does not have an influence on normalised quantities like k-ratios.

For all beam energies, the depth distributions obtained from the M_1-model match the MC

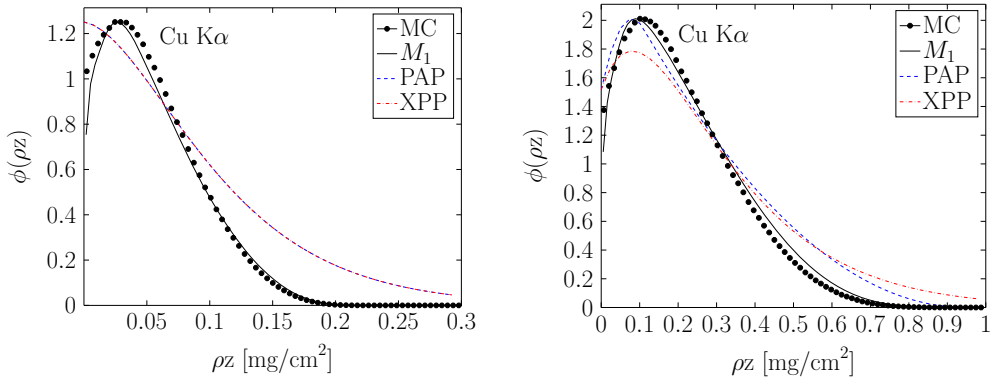

(a) 12 keV (b) 20 keV

Figure 2. Normalised depth distribution of Cu-Kα radiation ($\phi(\rho z)$) in copper at different beam energies. Comparison of the M_1 moment model to Monte Carlo and two common analytical models (XPP and PAP).

results very well. The results for XPP and PAP model approach the MC results for increasing beam energy but nevertheless clearly deviate from the MC results. The deviation is most evident near the sample surface for the lower beam energy of 12 keV where the graphs deviate also qualitatively, which reflects the limited applicability of the PAP and XPP model to cases in which the beam energy is close to the minimal excitation energy of the shell of interest [4].

4.2. Thin film

A common sample structure of interest are multi-layered samples. This motivates the material structure of our second test case, a thin film on a substrate. Both the substrate and the thin film consist of only one chemical element as visualised in the schematic drawing shown in Table 2. We look at two material combinations with nickel as substrate in both cases. We chose the material of the thin film to be chromium and aluminium in order to have, respectively, a moderate and a strong difference of the atomic number between both materials. These correspond respectively to the cases of a moderate and a strong change in material properties at the interface.

Analogous to the homogeneous test case, we validate the M_1-model based on the depth distributions of $K\alpha$-radiation, which are plotted in figs. 3(a) and 3(b). We computed the depth distribution of $K\alpha$-radiation neglecting the fact that each element is present only in either the thin film or the substrate. This is not physically correct but provides more information for comparison and can easily be corrected by ignoring the first or second part of the graph. As for the homogeneous test case, we scaled the M_1 and MC results such that the maximum Cr/Al $K\alpha$-radiation equals the respective maximum computed using the PAP model. The dashed vertical lines in figs. 3(a) and 3(b) indicate the position of the interface between the thin film and the substrate.

For the moderate case of chromium on nickel (fig. 3(a)), our observations are similar to the homogeneous case. We observe very good agreement between the M_1 and the MC results whereas the XPP and PAP results deviate significantly from the MC solution. The same applies to the depth distributions of Ni-$K\alpha$ radiation for the case of a thin aluminium film (fig. 3(b)). The M_1 results for the depth distribution of aluminium $K\alpha$-radiation start to deviate slightly from the MC results at a mass depth of around 0.1 mg/cm^2. Comparing the deviation with the deviations between the results for different elastic scattering cross-sections (screened Rutherford and Mott) we can see that the deviation is in the range of uncertainties due to material parameters. Even though the XPP and PAP results for the depth distribution of Al-$K\alpha$ radiation are relatively

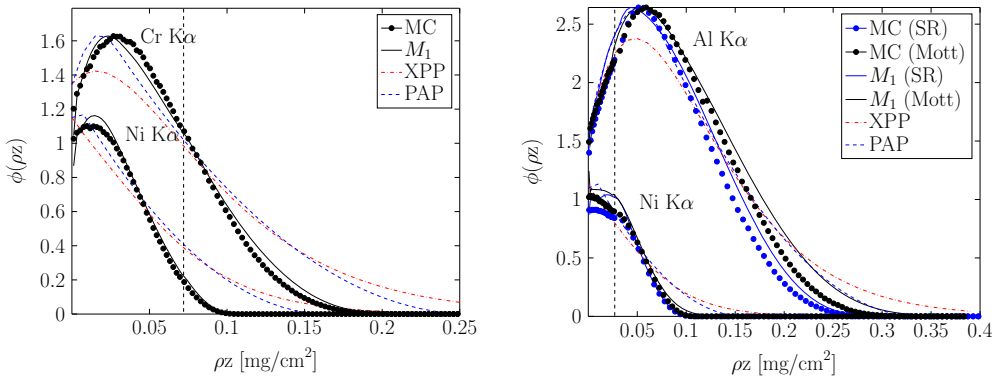

(a) Cr-Ni (b) Al-Ni

Figure 3. Depth distribution of Kα-radiation for two one layer thin film systems ((a) 100 nm chromium on nickel; (b) 100 nm aluminium on nickel) at 10 keV. Comparison of the M_1 moment model to Monte Carlo a two common analytical models (XPP and PAP).

good, the M_1 results are clearly better.

4.3. Interface setup

The third test case is also a binary structure. Two one-element materials separated vertically, with the interface aligned to the electron beam as visualised below. As the chemical composition of this sample is not a function of depth, classical analytical models like XPP and PAP are not applicable. We will, therefore, compare the M_1 solution with MC results only.

We will value the M_1 solution based on the spatial distribution of the electron number density n. A reference solution n_{ref} was calculated from a weighted histogram for the position and energy of electrons in a MC simulation. We used 100 bins to discretise the energy interval $[0, \epsilon_B]$ and a 100×100 equidistant grid to discretise the sample in space. A comparison of the electron number densities at different energies is presented in fig. 4. Comparing the M_1 with the Monte Carlo solution, we see that the M_1-model is able to reproduce the dynamics of the electrons very well. For both models, the electrons penetrate the chromium region ($x < 0$) about the same amount further then the nickel region ($x > 0$). The area occupied by electrons and the location of the maximum electron density for the different energies match remarkably well too. Furthermore, the M_1-model reproduces the sharp increase in density at the bottom. The main difference between both solutions is the earlier smoothing out of the electron density distribution towards the centre of the occupied region in the MC solution. This effect has to be investigated further.

Also noticeable in fig. 4 is the stochastic character of the Monte Carlo solution, resulting in a noisy solution even for a fairly high number of 200,000 simulated electrons. The distortion of the solution by the stochastic noise increases with decreasing energy (fig. 4), as the records in the histogram are distributed over more bins, which increases the uncertainty per bin. This effect makes the calculation of gradients, necessary for solving the inverse problem, difficult. As a deterministic model, the M_1 solution always gives smooth solutions, which are well suited for computing gradients.

5. Conclusion

Taking Monte Carlo as a reference, the results for the three test cases presented in the previous section show that the M_1-model is able to reproduce the electron dynamics in EPMA applications very well. Compared to classical analytical models like XPP and PAP, the M_1-model is more

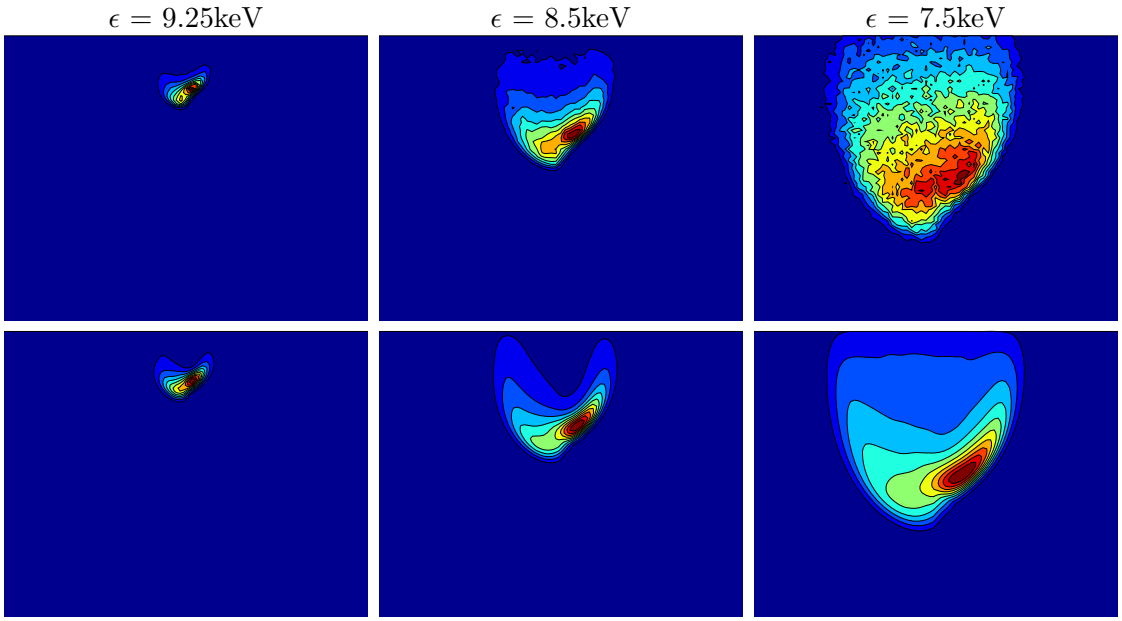

Figure 4. Spatial electron number density distribution in a binary structure (chromium (left) and nickel (right)) at different energies for a beam energy of $\epsilon_B = 10\,\text{keV}$. Comparison of the M_1 solution n_{M_1} (bottom) to Monte Carlo n_{ref} (top).

accurate and far more flexible. Nevertheless, the M_1-model is still an approximation to the BCSD equation and hence it is natural that M_1 solutions usually deviate slightly from MC solutions. Further investigations are necessary to better understand the cause of the deviations, the impact of such deviations on the accuracy of k-ratios and possible improvement through higher order moment models.

In summary, we are convinced that a minimum entropy moment model of the BCSD together with a sophisticated method for computing gradients of PDE constrained optimization problems (i.e., adjoint state method) is an efficient, flexible and accurate concept for solving the inverse problem of reconstructing the chemical material composition in EPMA.

References

[1] Tarantola A 2005 *Inverse problem theory and methods for model parameter estimation.* (Philadelphia, PA: Society for Industrial and Applied Mathematics)
[2] Aster R C, Borchers B and Thurber C H 2013 *Parameter estimation and inverse problems (Second Edition).* (Boston, MA: Academic Press)
[3] Bastin G F and Heijligers H J M 1991 Quantitative electron probe microanalysis of ultra-light elements (boron–oxygen). *Electron Probe Quantitation* (Heinrich K F J and Newbury D E, Eds.) (New York, NY: Plenum Press) 145–161
[4] Pouchou J L and Pichoir F 1991 Quantitative analysis of homogeneous or stratified microvolumes applying the model "PAP". *Electron Probe Quantitation* (Heinrich K F J and Newbury D E, Eds.) (New York, NY: Plenum Press) 31–75
[5] Bastin G F, Dijkstra J M and Heijligers H J M 1998 *X-ray Spectrom.* **27** 3–10
[6] Packwood R H and Brown J D 1981 *X-ray Spectrom.* **10** 138–146
[7] Philibert J 1963 A method for calculating the absorption correction in electron probe microanalysis. *X-ray optics and X-ray microanalysis* (Pattee H H, Coslett V E and Engström A, Eds.) (New York, NY: Springer) 379–392
[8] Love G, Sewell D A and Scott V D 1984 *J. Phys. Colloques* **45** 21–24
[9] Pouchou J L and Pichoir F 1984 *Rech. Aérospat.* **3** 167–192
[10] Ammann N and Karduck P 1990 A further developed Monte Carlo model for the quantitative EPMA of

complex samples. *Microbeam Analysis* (Michael J and Ingram P, Eds.) (San Francisco, CA: San Francisco Press) 150–154
[11] Gauvin R, Lifshin E, Demers H, Horny P and Campbell H 2006 *Microsc. Microanal.* **12** 49–64
[12] Joy D C 1991 *Scanning Microscopy* **5** 329–337
[13] Ritchie N W M 2005 *Surf. Interface Anal.* **37** 1006–1011
[14] Salvat F 2015 *PENELOPE-2014: a code system for Monte Carlo simulation of electron and photon transport.* (Issy-Les-Moulinex, France: OECD-NEA)
[15] Fathers D and Rez P 1979 Transport equation theory of electron backscattering. *Scanning Electron Microscopy* (Johari O, Ed.) (AMF O'Hare, IL: SEM, Inc.) pp 55–66
[16] Case K and Zweifel P 1967 *Linear transport theory* (Boston, MA: Addison-Wesley)
[17] Frank M, Herty M and Sandjo A N 2010 *Math. Models Methods Appl. Sci.* **20** 661–678
[18] Küpper K 2016 *Models, numerical methods, and uncertainty quantification for radiation therapy.* PhD-thesis (Aachen, Germany: RWTH Aachen University)
[19] Duclous R, Dubroca B and Frank M 2010 *Phys. Med. Biol.* **55** 3843–3857
[20] Pichard T 2016 *Mathematical modelling for dose depositon in photon therapy.* PhD-thesis (Bordeaux, France: Université de Bordeaux)
[21] Olbrant E 2012 *Models and numerical methods for time- and energy-dependent particle transport.* PhD-thesis (Aachen, Germany: RWTH Aachen University)
[22] Ammann N 1989 *Monte Carlo simulation der röntgenstrahlungs - Erzeugung durch elektronenbeschuß in schicht - Substrat - Systemen.* MSc-thesis (Aachen, Germany: RWTH Aachen University)
[23] Ritchie N W M 2009 *Micros. Microanal.* **15** 454–522
[24] Mevenkamp N 2013 *Inverse modeling in electron probe microanalysis based on deterministic transport equations.* MSc-thesis (Aachen, Germany: RWTH Aachen University)
[25] LeVeque R J 1992 *Numerical methods for conservation laws* 2nd ed (Basel, Switzerland: Birkhäuser)
[26] Cockburn B and Shu C W 1989 *Math. Comput.* **52** 411–435
[27] Cockburn B, Lin S Y and Shu C W 1989 *J. Comput. Phys.* **84** 90–113
[28] Cockburn B, Hou S and Shu C W 1990 *Math. Comput.* **54** 545–581
[29] Bangerth W, Davydov D, Heister T, Heltai L, Kanschat G, Kronbichler M, Maier M, Turcksin B and Wells D 2016 *J. Numer. Math.* **24** 135–141
[30] Bangerth W, Hartmann R and Kanschat G 2007 *ACM Trans. Math. Softw.* **33** 24/1–24/27
[31] Reimer L 1998 *Scanning electron microscopy* 2nd ed (Berlin: Springer)
[32] Powell C, Salvat F and Jablonski A 2007 *NIST electron elastic-scattering cross-section database* (Gaithersburg, MD: National Institute of Standards and Technology)
[33] McKinley W A and Feshbach H 1948 *Phys. Rev.* **74** 1759–1769
[34] Berger M J and Seltzer S M 1964 *NASA Special Publication* **3012**
[35] Casnati E, Tartari A and Baraldi C 1982 *J. Phys. B: At. Mol. Opt. Phys.* **16** 505
[36] Cullen D E, Hubbell J H and Kissel L 1997 *EPDL97 The Evaluated Data Library '97 Version.* (Livermore, CA: Lawrence Livermore National Laboratory)